© 2024 Institute of Theoretical Physics CAS, Chinese Physical Society and IOP Publishing Printed in China

Commun. Theor. Phys. **76** (2024) 085402 (15pp) https://doi.org/10.1088/1572-9494/ad4ce0

Observational appearances of hairy black holes in the framework of gravitational decoupling

Yizhi Liang, Xin Lyu and Jun Tao*

Center for Theoretical Physics, College of Physics, Sichuan University, Chengdu 610065, China

E-mail: liangyizhi@stu.scu.edu.cn, lyuxin@stu.scu.edu.cn and taojun@scu.edu.cn

Received 27 March 2024, revised 16 May 2024
Accepted for publication 17 May 2024
Published 3 July 2024

Abstract

We investigate the observational appearance of static and spherically symmetric hairy black holes in the framework of gravitational decoupling with the weak energy condition (WEC). Two types of thin illumination conditions are studied: spherical accretion and disk accretion. As the hairy parameter increases, the size of the photon sphere and photon rings in both models decreases, and the overall luminosity attenuation becomes more pronounced. In spherical accretion, the luminosity of infalling accretion is significantly lower than that of stationary accretion. In disk accretion the luminosity of the black hole is contributed by direct emission, the lensing ring and the photon ring. Employing four types of astrophysical disk luminosity model, we investigate the appearance of halos and note that their luminosities do not superimpose when the source is on or beyond the innermost stable circular orbit.

Keywords: hairy black hole, shadow, gravitational decoupling, accretion disk

(Some figures may appear in colour only in the online journal)

1. Introduction

Recently, the Event Horizon Telescope (EHT) Collaboration unveiled images of the supermassive black hole situated at the center of our galaxy [1–6]. These depictions consistently exhibit a luminous ring encircling a central dark region, similar to the M87* black hole images reported in 2019 [7–12]. In the presence of a light source behind or around the black hole, certain photons fall into the black hole, forming a central dark region known as the black hole shadow, while some undergo deflection, generating a radiant ring around the black hole shadow, referred to as the photon sphere [13]. The investigation of black hole shadows started from a Schwarzschild black hole [14]. Then Bardeen *et al* explored the shadow of a Kerr black hole [15]. Numerical calculation of the black hole shadow with a rotating accretion disk was started in [16]. The visible shapes of the brightest black holes accompanied by an accretion disk were comparable with the EHT observations for M87* and SgrA* [17, 18]. In recent years, research on black hole shadows has extended to black holes in Born–Infeld electromagnetic fields [19, 20], the Ayón–Beato–García black hole family [21] and black holes with multiple photon spheres [22–25]. Moreover, Euler–Heisenberg black holes [26], black holes immersed in quintessence dark energy [27], brane-world black holes [28] and others have also been studied [29–33]. Black hole shadows are important for verifying general relativity in strong gravitational fields and for studying cold dark matter perturbations in the early universe [34].

The ultimate phase of gravitational collapse is theorized to result in the formation of a Kerr–Newman black hole, regardless of the nature of the pre-existing objects involved in the collapse. This proposition implies that these outcomes can be uniquely defined based on their mass, angular momentum and charge properties [35]. The current view is that hairy black holes exist, described not only by mass, charge and angular momentum but also by some nonlinear fields or sources. One can consider a static hairy black hole, which is reasonable because the energy and angular momentum for a rotating one can be extracted by the Penrose superradiance

* Author to whom any correspondence should be addressed.

process [36, 37] or the Blandford and Znajek mechanism [38]. Thus, the existence of non-rotating hairy black holes cannot be ignored. The hairy black hole solution is not easy to find because obtaining analytical solutions directly for the Einstein field equations is challenging. However, a notable exception that allows for direct solutions is the perfect fluid $\tilde{T}_{\mu\nu}$. Therefore, we consider employing the method of minimal geometric deformation (MGD) applied in brane-world scenarios [39, 40], which involves separately addressing and solving each term of the gravitational source in the equations. This provides a powerful tool for solving Einstein's field equations under nonlinear conditions. The MGD method is widely used in gravitational decoupling and has been verified by several problems in relativistic astrophysics [41–44]. Then a new static spherically symmetric hairy black hole solution is investigated by using gravitational decoupling [45–53].

To conduct our analysis, we will appropriately employ two types of accretion models, namely spherical accretion and disk accretion [54, 55]. Spherical accretion comprises stationary and infalling accretion. The former simulates the luminosity from a quiescent accretion flow while the latter simulates the luminosity from accretion flow radially infalling into the black hole. Disk accretion models include the exponential model, power-law exponential model, bell-shaped model and GLM model. In this context, the radiation from the exponential, power-law and bell-shaped models emanates respectively from the innermost stable circular orbit, the photon sphere and the event horizon. These models are considered to be in accordance with the observational evidence. Besides, the GLM model has been used in recent studies of general relativistic magnetohydrodynamic simulations of accretion flows [56]: under mild astrophysical assumptions, illuminated by a thin accretion disk, the photon rings are broken into an infinite sequence of concentric rings. These rings produce similar features on the observer's detector, potentially allowing differentiation between different black hole metrics [57]. However, due to the exponential decrease in their luminosities, inner rings are challenging to observe. In this paper, we theoretically predict the observed images of photon rings of hairy black holes under weak energy conditions (WEC). These might be observable in future instruments such as the next-generation Event Horizon Telescope [58].

This paper is organized as follows. In section 2, we briefly review the method of gravitational decoupling and the work of Avalos and derive the black hole metric in WEC, then we derive the photon equation of motion and plot the trajectories for different values of the hairy parameter α. Then, in section 3, we investigate the relationship between the light intensity I with respect to the radius r as well as the impact parameter b, and use the backward ray-tracing method to investigate the appearance of stationary and infalling accretion disks. Afterwards, in section 4, we use the same method to simulate the shadows of the accretion disk under five different emission models. Finally, we outline our conclusions and present some perspectives for the future in section 5.

2. Gravitational decoupling and geodesics

In this section, we present the concept of a hairy black hole in the framework of gravitational decoupling and proceed to examine the trajectories of massless and massive particles. In the case of spherically symmetric and stationary spacetime, an ansatz can be formulated

$$\mathrm{d}s^2 = -\mathrm{e}^{\nu(r)}\mathrm{d}t^2 + \mathrm{e}^{\lambda(r)}\mathrm{d}r^2 + r^2\mathrm{d}\Omega^2, \tag{1}$$

where $\mathrm{d}\Omega^2 = \mathrm{d}\theta^2 + \sin^2\theta\mathrm{d}\phi^2$. We can obtain the metric function [45]

$$F(r) = \mathrm{e}^{\nu} = \mathrm{e}^{-\lambda} = 1 - \frac{2M}{r} + \frac{5}{4}\frac{\alpha M}{r^2} + \frac{\alpha M}{r^2}\ln\frac{r}{r_H}, \tag{2}$$

where M is the mass of the black hole, α is the hairy parameter, which represents the matter sector, r_H is the horizon radius, which has the form $r_H = M + \sqrt{M^2 - 5/4\alpha\mathrm{M}}$, and $0 < \alpha < 0.8M$ is necessary to avoid the appearance of a naked singularity.

To conduct our investigation on the shadow of the black hole, it is natural to concentrate on the trajectory of the photons in the background spacetime. The equation of motion of the massless particles can be demonstrated as

$$-g_{\mu\nu}\frac{\mathrm{d}x^{\mu}}{\mathrm{d}\lambda}\frac{\mathrm{d}x^{\nu}}{\mathrm{d}\lambda} = 0, \tag{3}$$

where λ is the affine parameter. We are more concerned with spherically symmetric spacetime, and one can find two Killing vectors

$$\begin{aligned} K_{\mu} &= (-F(r),\, 0,\, 0,\, 0), \\ R_{\mu} &= (0,\, 0,\, 0,\, r^2\sin^2\theta). \end{aligned} \tag{4}$$

We could obtain the energy E and the angular momentum L for $\theta = \pi/2$ along the geodesics

$$E = -K_{\mu}\frac{\mathrm{d}x^{\mu}}{\mathrm{d}\lambda} = F(r)\frac{\mathrm{d}t}{\mathrm{d}\lambda}, \quad L = R_{\mu}\frac{\mathrm{d}x^{\mu}}{\mathrm{d}\lambda} = r^2\frac{\mathrm{d}\phi}{\mathrm{d}\lambda}. \tag{5}$$

Then the geodesics equation (3) can be rewritten as

$$-E^2 + F(r)\frac{L^2}{r^2} + \left(\frac{\mathrm{d}r}{\mathrm{d}\lambda}\right)^2 = 0. \tag{6}$$

By setting the affine parameter λ into λ/L and defining the impact parameter $b \equiv L/E$, one can derive

$$\dot{t} = \frac{1}{bF(r)}, \tag{7}$$

$$\dot{\phi} = \pm\frac{1}{r^2}, \tag{8}$$

$$\dot{r}^2 = \frac{1}{b^2} - \frac{F(r)}{r^2}, \tag{9}$$

where the $\pm$ denotes the counterclockwise and clockwise geodesics of the photon. Subsequently, the equation for the trajectory of the photon can be deduced as

$$\frac{\mathrm{d}r}{\mathrm{d}\phi} = \pm r^2\sqrt{\frac{1}{b^2} - \frac{F(r)}{r^2}}. \tag{10}$$

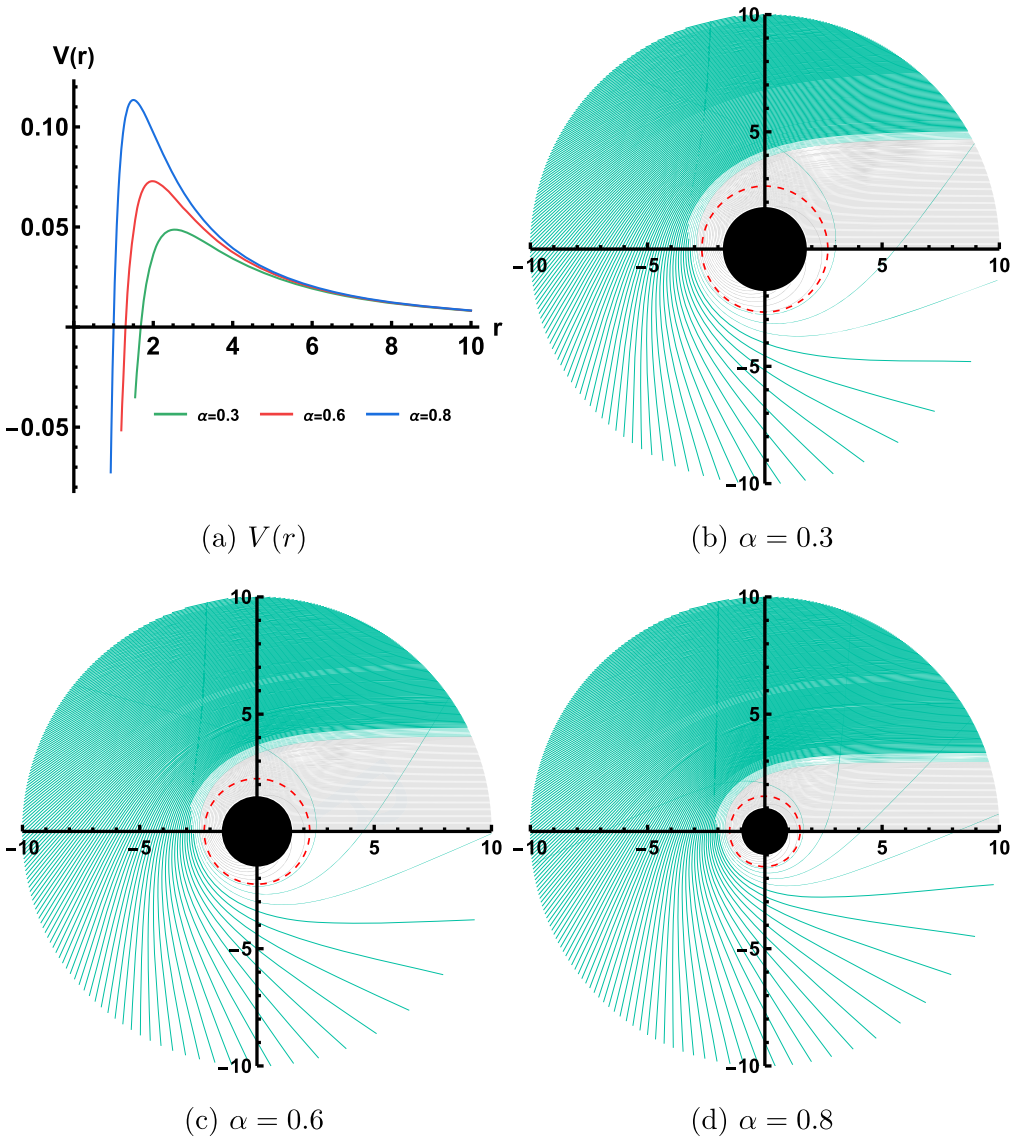

(a) $V(r)$ (b) $\alpha = 0.3$

(c) $\alpha = 0.6$ (d) $\alpha = 0.8$

Figure 1. The plot on the upper left is the effective potential $V(r)$ of photon with respect to the radius r. The green, red and blue lines represent $V(r)$ differing in the hairy parameter α. The other parts show the geodesic of photons for different α with fixed $M = 1$, where the green lines are the photons escaping from the black hole, the gray ones are photons falling in the black hole and the red dashed line indicates the photon sphere.

One can set $V(r) = F(r)/r^2$ as the effective potential of photons, which is shown in figure 1(a), and notice that when $\dot{r}|_{r=r_{\rm ph}} = 0$, $\ddot{r}|_{r=r_{\rm ph}} = 0$ photons can circle the black hole many times in unstable orbits, called the photon sphere, which satisfy

$$b_{\rm ph} = \frac{1}{\sqrt{V(r_{\rm ph})}}, \qquad \frac{{\rm d}V(r_{\rm ph})}{{\rm d}r} = 0, \qquad \frac{{\rm d}^2V(r_{\rm ph})}{{\rm d}r^2} \leqslant 0. \tag{11}$$

We can obtain the figures of different parameters of the photon trajectory by numerically integrating equation (10), as shown in figures 1(b)–(d) with different α. The green lines indicate photons that escape the black hole after being affected by its gravity, and the gray lines are photons that fall into the black hole. The red dashed line indicates the photon sphere, which is a very ideal situation. Note that the photon sphere is the division between photons that fall into the black hole and those that escape from the black hole.

Then we consider particles with unit mass. The geodesic equation implying the trajectories of particles with unit mass can be simply written as

$$-g_{\mu\nu}\frac{{\rm d}x^\mu}{{\rm d}\lambda}\frac{{\rm d}x^\nu}{{\rm d}\lambda} = 1, \tag{12}$$

where τ is the proper time of the particles. Similar to photons, one can derive the equation of motion in spacetime [59]

$$\left(\frac{{\rm d}r}{{\rm d}\tau}\right)^2 = E_m^2 - F(r)\left(1 + \frac{L_m^2}{r^2}\right), \tag{13}$$

where E_m and L_m are the energy and angular momentum of the particle, respectively. Unlike for the definition of the effective potential of photons, we can simply set the effective

Table 1. Data for $r_{\rm h}$, $r_{\rm ph}$, $b_{\rm ph}$ and $r_{\rm ISCO}$ for different α with fixed $M = 1$. For $\alpha \to 0$, the black hole reduces to the Schwarzschild type.

	$\alpha = 0$	$\alpha = 0.3$	$\alpha = 0.4$	$\alpha = 0.5$	$\alpha = 0.6$	$\alpha = 0.7$
$r_{\rm h}$	2	1.790 57	1.707 11	1.612 37	1.5	1.353 55
$r_{\rm ph}$	3	2.686 04	2.5692	2.418 91	2.250 46	2.030 96
$b_{\rm ph}$	5.196 15	4.717 08	4.527 07	4.312 21	4.058 74	3.731 48
$r_{\rm ISCO}$	6	5.271 45	4.984 17	4.660 41	4.279 80	3.789 92

potential of the massive particle

$$V_{\rm eff}(r) = \sqrt{F(r)\left(1 + \frac{L_m^2}{r^2}\right)}. \tag{14}$$

There is a minimum radius at which stable circular motion remains feasible, defined as the innermost stable circular orbit (ISCO), and it satisfies

$$\frac{{\rm d}r}{{\rm d}\tau} = 0, \qquad \frac{{\rm d}^2 r}{{\rm d}\tau^2} = 0. \tag{15}$$

Due to the complexity of the analytical solutions of $r_{\rm h}$, $r_{\rm ph}$, $b_{\rm ph}$ and $r_{\rm ISCO}$ we list the numerical solutions in table 1.

Note that as the hairy parameter α increases, $r_{\rm h}$, $r_{\rm ph}$ and $r_{\rm ISCO}$ all decrease, and fewer photons fall into the black hole. As the impact parameter b is in a fixed interval, an increase in α causes the particles to undergo large-angle deflection. The effect of α is significant for the observational appearance.

3. Shadows and photon spheres with spherical accretions

A black hole accretes matter, which becomes the source of illumination. In this section, we study spherically symmetric accretion flows, categorized as stationary accretion and infalling accretion. The backward ray-tracing method is employed to study the specific intensity received by a distant observer [16].

3.1. Stationary spherical accretions

We start with the investigation of the hairy black hole shadows of stationary spherically symmetric accretions, and are generally concerned with the specific intensity observed by the static observer. The photon emissivity can be written as

$$j(\nu_{\rm e}) \propto \rho(r) P(\nu_{\rm e}), \tag{16}$$

where $\rho(r)$ is the photon density. We assume that the density $\rho(r)$ satisfies the logarithmic normal distribution due to spherical symmetry; this can be expressed as

$$\rho(r) = \frac{1}{r}\sqrt{\frac{\gamma}{\pi}} {\rm e}^{-\gamma \ln^2 \frac{r}{r_m}}, \tag{17}$$

The parameter γ determines the rate at which the photon density decays in relation to the distance from the sources and $r_m = r_{\rm ph} {\rm e}^{\frac{1}{2\gamma}}$ is a parameter of the logarithmic normal distribution.

One can employ a non-monochromatic light source satisfying a normal distribution with center frequency ν_c, and $P(\nu_c) = \int_{\nu_c+\sqrt{2}\sigma}^{\nu_c-\sqrt{2}\sigma} \frac{1}{\sigma\sqrt{2\pi}} {\rm e}^{-\frac{(\nu-\nu_c)^2}{2\sigma^2}} {\rm d}\nu \approx 0.842\,70$. By integrating equation (16) along the null geodesic, the specific light intensity observed by the observer reads as [60]

$$I(b) = \int g^3 j(\nu_{\rm e}) {\rm d}l_{\rm prop}. \tag{18}$$

Here g is the redshift factor and ${\rm d}l_{\rm prop}$ is the infinitesimal proper line element. The infinitesimal proper length reads

$${\rm d}l_{\rm prop} = \pm\sqrt{g_{ij}{\rm d}x^i {\rm d}x^j} = \pm\sqrt{\frac{1}{F(r)} + r^2\left(\frac{{\rm d}\phi}{{\rm d}r}\right)^2}\,{\rm d}r, \tag{19}$$

where the plus and minus signs of the fourth term indicate the photon's counterclockwise and clockwise motions, respectively. The redshift factor g can be determined by $g = p_\alpha u_{\rm o}^\alpha / p_\beta u_{\rm e}^\beta$, where p_α and p_β are the four-momentum of the photon at reception and emission and u_o^α and u_o^β are the four-velocity of the observer and the accretion disk. Since the observer is located at an infinite distance, we have $g_{\mu\nu} u_e^\mu u_e^\nu = 1$ and then $u_{\rm o}^\alpha = (1, 0, 0, 0)$, $u_{\rm e}^\beta = (\sqrt{1/F(r)}, 0, 0, 0)$. By substituting $p_t = -E$ into $g_{\mu\nu} p_e^\mu p_e^\nu = 0$, one can obtain

$$p_\mu = \left(-1, \pm\sqrt{\frac{1}{F(r)}\left(\frac{1}{F(r)} - \frac{b^2}{r^2}\right)}, 0, \pm b\right), \tag{20}$$

where the $\pm$ signs of the second term indicate the radial inward and outward motion of the photon, respectively.

The specific intensity I with respect to the impact parameter b can be obtained by substituting equation (16) and equation (19) into equation (18). We set $\gamma = 1$ and $M = 1$ for simplicity. The blue line in the left column of figure 2 represents the specific intensity $I(b)$ with respect to the impact parameter b. Therefore, we can obtain the shadow of a black hole with a static spherical accretion disk numerically by calculating equation (18) in figures 2(c), (f) and (i), corresponding to $\alpha = 0.3$, 0.6 and 0.8, respectively. The color distribution in the diagrams represents the trend of $I(b)$ with b.

One can see that the luminosity of stationary spherical accretion peaks near the photon sphere. As the hairy parameter α increases, the overall luminosity of stationary accretion decreases. The intensity inside the photon sphere does not completely disappear because some photons escape the black hole. Therefore, the shadow region of the black hole on the observer's screen is not completely dark [61].

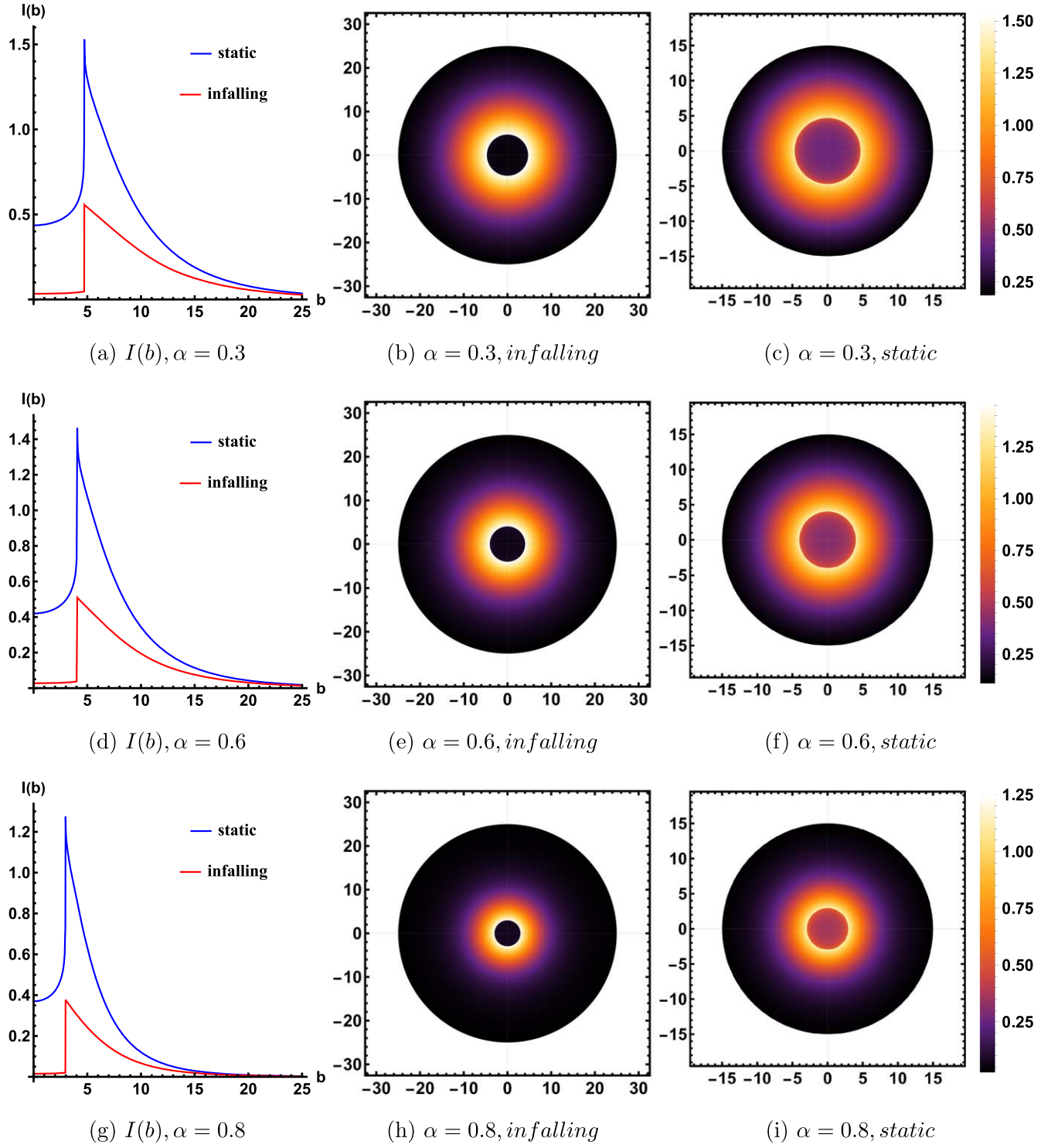

Figure 2. Stationary and infalling spherical accretions with $\alpha = 0.3$, $\alpha = 0.6$ and $\alpha = 0.8$ and fixed $M = 1$, $\gamma = 1$. The blue line in the plots in the left column represents the specific light intensity for static accretion and the red line represents the specific light intensity for infalling accretion. The two-dimensional diagrams in the middle column are for infalling accretion, while the two-dimensional diagrams on the right are for static accretion.

3.2. Infalling spherical accretions

Accretion matter is always dynamic, and it is meaningful to study the shadows as well as the photon sphere of a black hole by the infalling spherical accretions. Similar to the stationary situation, we use equation (18) to describe the intensities of the shadows, and the redshift factor g has been investigated before. The four-velocity of the infalling accretion can be expressed as

$$u_{\mathrm{e}}^{\beta} = \left(\frac{1}{F(r)}, -\sqrt{1 - F(r)}, 0, 0\right), \tag{21}$$

Table 2. The ranges of impact parameter b with respect to direct emission, lensing ring and photon ring for different α and fixed $M = 1$.

	Direct emission, $n < 3/4$	Lensing ring, $3/4 < n < 5/4$	Photon ring, $n > 5/4$
$\alpha = 0.3$	$0 \leqslant b < 4.54143$, $b > 5.61601$	$4.54143 < b < 4.70773$, $4.74535 < b < 5.61601$	$4.70773 < b < 4.74535$
$\alpha = 0.6$	$0 \leqslant b < 3.88749$, $b > 4.96069$	$3.88749 < b < 4.04903$, $4.08953 < b < 4.96069$	$4.04903 < b < 4.08953$
$\alpha = 0.8$	$0 \leqslant b < 2.78218$, $b > 4.02983$	$2.78218 < b < 2.95654$, $3.01789 < b < 4.02983$	$2.95654 < b < 3.01789$

then we can derive the expression for the redshift factor as

$$g = \frac{F(r)}{1 \pm F(r)\sqrt{1 - F(r)}\sqrt{1 - \frac{F(r)b^2}{r^2}}}, \tag{22}$$

where the $\pm$ indicates a photon moving inward and outward, respectively. Red lines in figures 2(a), (d) and (g) show the specific intensity of infalling accretion, and figures 2(b), (e) and (h) demonstrate the luminance distribution of photons hitting the receiving screen for observers.

Comparing the simulated illustrations of static and infalling accretion, we find some interesting facts. The specific light intensities of static and infalling accretion reach a maximum at the same impact parameter b. Subsequently, the specific light intensity of static accretion undergoes a significant decay, while that of infalling accretion is relatively mild; eventually they both converge to zero at infinity. Compared with stationary accretion, the luminosity of infalling accretion is slightly lower, attributed to the smaller redshift factor for matter falling into the accretion. As α increases, the overall luminosity of infalling accretion decreases.

4. Shadow and rings of a black hole with thin accretion

In this section we study thin disk accretion models of a hairy black hole in WEC. One can treat the accreted matter as the light source and study the shadow. Due to the rotation, accretion disks around massive celestial objects are typically located at the equatorial plane. If we consider an observer at infinity along the equatorial plane, details of the black hole's halo would be challenging to discern. For simplicity, we contemplate an observer at infinity perpendicular to the equatorial plane.

4.1. Observed specific intensities and transfer functions

Inspired by [60], we could use the orbital plane azimuthal angle ϕ to define the total number of orbits $n = \phi/2\pi$, which depends on the impact parameter b. According to the different values of n, orbits can be categorized into distinct types: direct emission occurs when $n < 3/4$, resulting in a single intersection with the accretion disk; a lensing ring is formed when $3/4 < n < 5/4$, leading to photons passing through the accretion disk twice; and a photon ring is established when $n > 5/4$, causing photons to traverse the accretion disk more than three times.

The range of the impact parameter b with respect to direct emission, a lensing ring and a photon ring are shown in table 2, and the visible appearance is shown in figure 3. In the upper row, the lines in red, blue and green represent direct emission, lensing ring and photon ring photons, respectively. Direct emission with a lower orbital number accounts for a large fraction of the photons, followed by the lensing ring, while the photon ring with the highest orbital number has rather few photons. At the same time, we find that the impact parameter of the photons in the lensing ring and photon ring decreases significantly as the hairy parameter α increases. In the lower row, we categorize the photons according to the number of orbits, redrawing the geodesic diagrams with the corresponding red, blue and green colors. We note with interest that an increase in α does not affect the proportional distribution of photons for the three orbital numbers, but it causes a decrease in the impact parameter b for the photon ring. This is a significant difference from several previously discovered hairy black holes [33, 62].

It is assumed that the disk lies in the equatorial plane and the emissions from it are isotropic. The observed specific intensity with frequency ν_e can be written as [63]

$$I_{\rm o}(\nu_{\rm o}, r) = g^3 I_{\rm e}(\nu_{\rm e}, r), \tag{23}$$

where $\nu_{\rm o}$ is the observed photon frequency and $I_{\rm e}$ is the emitted specific intensity [32]. The total observed specific intensity can be expressed as

$$I(r) = \int I_{\rm o}(r){\rm d}\nu = F^2(r) I_{\rm e}(r). \tag{24}$$

Since the thin disk is located in the equatorial plane, the photons emitted from the north pole will intersect the disk, and it will capture brightness each time it intersects. The total observed intensity should be considered as the sum of these intensities from each intersection, which can be reexpressed as

$$I(r) = F^2(r) \sum_n I_{\rm e}(r)|_{r=r_n(b)}, \tag{25}$$

where $r_n(b)$ is the transfer function with $n = 1, 2, \ldots$. At each b, the slope of the transfer function ${\rm d}r/{\rm d}b$ represents the demagnification factor. We plot the first three transfer functions $r_n(b)$ in figure 4. The red, blue and green lines correspond to the transfer function of $n = 1$, 2 and 3, respectively. The slope of $r_1(b)$ is close to 1, which is considered to be associated with the redshift source. The slope of $r_2(b)$ is high, indicating that the lensing ring is the

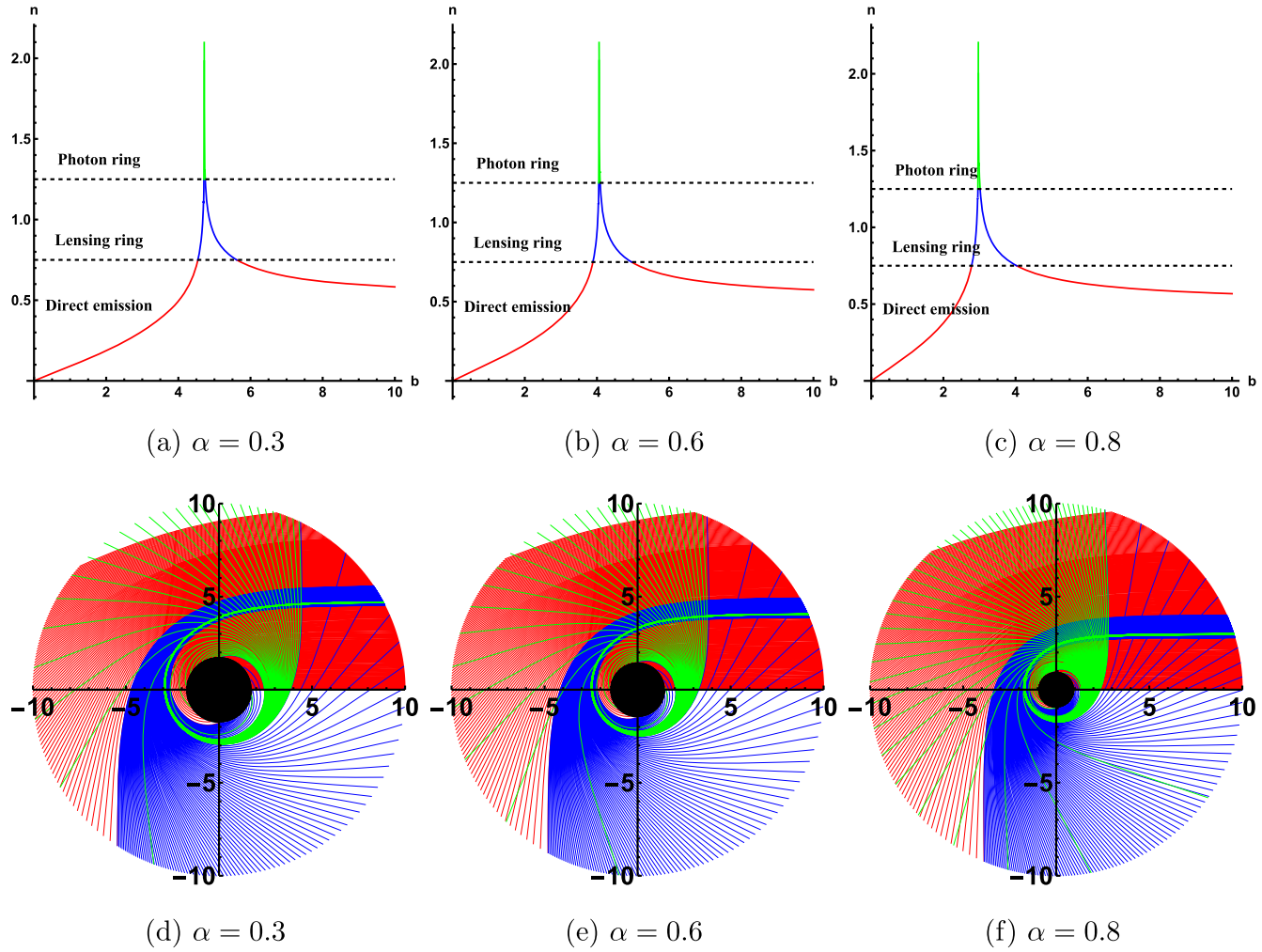

Figure 3. The visible ranges of direct emission, lensing ring and photon ring with respect to the impact parameter b. According to the number of loops, we replotted the geodesics. The red, blue and green lines are photons corresponding to direct emission, lensing ring and photon ring separately.

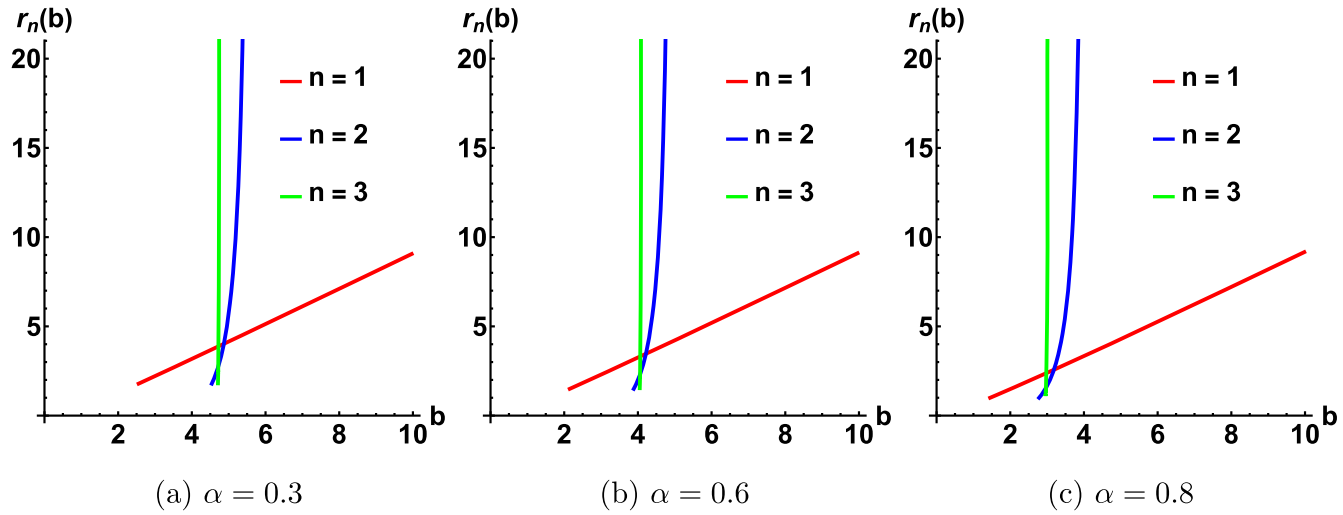

Figure 4. The three transfer functions of a hairy black hole in WEC with a thin accretion disk. The red, blue and green lines represent the first, second and third transfer functions, respectively.

demagnified image of the backside of the accretion disk. The slope of $r_3(b)$ approaches infinity, suggesting that the photon ring is the extremely demagnified image of the accretion disk, and higher-order transfer functions theoretically exist but their low luminosity makes them almost impossible to observe.

4.2. Observational appearances

In this subsection, we will consider four emission models to work out the optical appearances of a hairy black hole in WEC. One can focus on four different emission positions of the accretion disk: ISCO, the photon sphere radius $r_{\rm ph}$, the event horizon $r_{\rm h}$ [19] and a certain position $r = 17/3$ outside the ISCO [55]. The first three positions are special and have applications in many articles studying black hole shadows. In contrast, $17/3$ is a random position located beyond the innermost stabilizing circular orbit of the black hole, which is a very common situation, representing the emission of photons from matter on the accretion disk beyond the ISCO. We choose the GLM model to study this random position, considered by some of the literature to be the emission model that fits the observational reality [55]. These idealized models may not accurately represent reality but can still offer valuable perspectives on research into black hole shadow observations.

4.2.1. Exponential model. We employ the exponential model, whose emission of the accretion disk starts and peaks at the innermost stable circular orbit $r_{\rm ISCO}$. The emission intensity is distributed exponentially with the radial coordinate r, which has a very sharp decay after the peak presented in figures 5(a)–(c). The formula is

$$I_{\rm e1}(r)\Big/I_0 = \begin{cases} \exp\left[-(r - r_{\rm ISCO})\right], & r \geqslant r_{\rm ISCO}, \\ 0, & r < r_{\rm ISCO}, \end{cases} \tag{26}$$

where I_0 is the maximum intensity. $I_{\rm e1}$ has a very sharp decay after the peak, as shown in figures 5(a)–(c). For different α, there are three separate peaks observed in the specific light intensity, each corresponding to the intensities of direct emission, lensing ring and photon ring, respectively. These peaks are independent of each other and do not exhibit any superposition effects. For the cases with $\alpha = 0.3$, 0.6 and 0.8, direct emission experiences sharp changes at $b \approx 6.2$, 5.0 and 3.2, respectively. As a result of gravitational lensing effects, the intensity of the lensing ring is concentrated within a limited spectrum, which peaks at $b \approx 5.0$, 4.2 and 3.3. Photon ring intensity is a very narrow peak with $b \approx 4.6$, 4.0 and 3.0, contributing negligibly to the overall observed intensity.

The diagrams with respect to the special intensities are shown in figures 5(g)–(i), and the accretion structure are shown in figures 5(j)–(l). Within the brightest ring we can identify a sub-ring known as the lensing ring. Upon magnification, a very narrow photon ring is observed within the lensing ring. The overall brightness and width of the shadow are largely determined by direct emission. As the hairy parameter α increases, the overall luminosity of the accretion disk decreases and the lensing ring gets closer to direct emission. When $\alpha = 0.8$, one can observe that coupling occurs between the lensing ring and direct emission, resulting in a significant emission peak due to the superposition of their intensities. As there is incomplete coupling between the direct emission and the lensing ring, we can still clearly see the photon ring by zooming in on figure 5(l).

4.2.2. Power-law exponential model. In this section we consider the exponential model for emission, but the difference from the normal exponential model is that we choose the start as well as the peak intensity at the photon sphere. The expression is

$$I_{\rm e2}(r)/I_0 = \begin{cases} \frac{1}{r - r_{\rm ph} + 1} \exp\left[-(r - r_{\rm ph})\right], & r \geqslant r_{\rm ph}, \\ 0, & r < r_{\rm ph}, \end{cases} \tag{27}$$

where I_0 represents the maximum normalized intensity. Note that the difference between this model and the previous one is that the observation intensity only peaks at two b values, which indicates that the three intensities are not independent of each other. The first peaks, located at $b \approx 3.5$, 3.0 and 2.0 with respect to $\alpha = 0.3$, 0.6 and 0.8, are contributed only by the direct intensity. Furthermore, the second peaks are located at $b \approx 4.9$, 4.2 and 3.0 with respect to $\alpha = 0.3$, 0.6 and 0.8, which are contributed by all three intensities.

Two-dimensional representations of the total observed intensities can be found in figures 6 (g)–(i). The conjunction of the lensing ring and photon ring results in the creation of a notably bright yet exceptionally slender halo, with the two emissions being indistinguishable from each other. The direct emission exhibits a broader range despite having a lower observed intensity. In this theoretical framework, the overall brightness of the shadow is predominantly determined by the interaction between the photon ring and the lensing ring, with the direct emission mainly affecting the width of the shadow. As the hairy parameter α increases there is no significant decrease in the overall luminosity of the accretion disk. However, the size of rings undergoes a noticeable reduction.

4.2.3. Bell-shaped model. Furthermore, with the assumption that the emission extends continuously to the outer event horizon r_h, one can have the emission function moderately attenuated with a maximum at r_h, and the explicit expression is given as

$$I_{\rm e3}(r)\Big/I_0 = \begin{cases} \frac{1 - \tanh\left[r - (r_{\rm ISCO} - r_{\rm h} + 0.5)\right]}{1 - \tanh\left[r_{\rm h} - (r_{\rm ISCO} - r_{\rm h} + 0.5)\right]}, & r \geqslant r_{\rm h}, \\ 0, & r < r_{\rm h}, \end{cases} \tag{28}$$

where I_0 is also the maximum intensity. In figures 7(a)–(c), compared with the exponential and power-law exponential model, the direct emission intensities meet no abrupt end at any impact parameter b. They start from $b \approx 3.5$, 2.9 and 2.0 with respect to $\alpha = 0.3$, 0.6 and 0.8, and photon ring emission intensities hold at $b \approx 4.8$, 4.0 and 2.9 while the lensing ring emission exists as $b \in (4.7, 5.1)$, $(4.1, 4.5)$ and $(2.8, 3.4)$ [54].

Two-dimensional representations of the total observed intensities are presented in figures 7(g)–(i). Similar to the power-law model, the lensing ring and the photon ring together create a thin and bright halo, while the direct emission forms a relatively dim but broader halo. The lensing ring is more pronounced, but direct emission still dominates while the photon ring remains insignificantly small. As the hairy parameter α increases, there is a significant decrease in the overall luminosity of the accretion disk, accompanied by a noticeable reduction in the size of the rings.

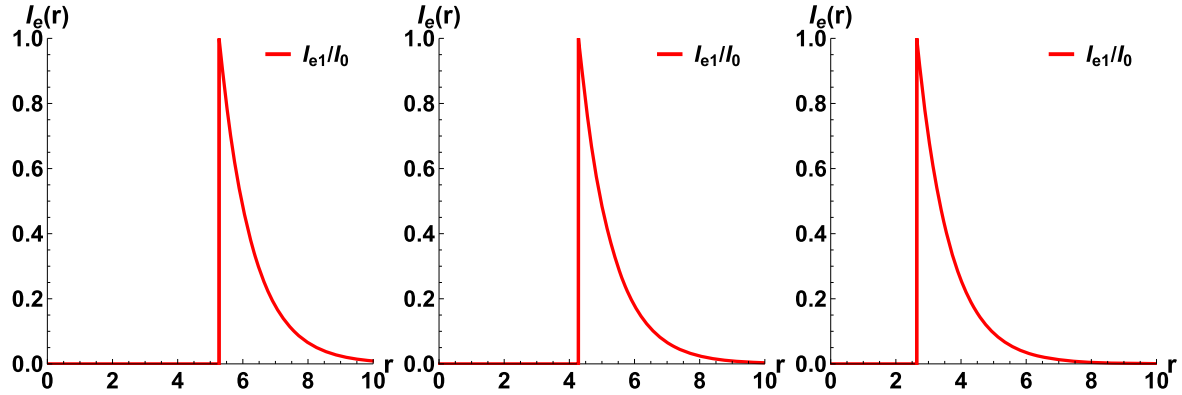

(a) $Ie, \alpha = 0.3$ (b) $Ie, \alpha = 0.6$ (c) $Ie, \alpha = 0.8$

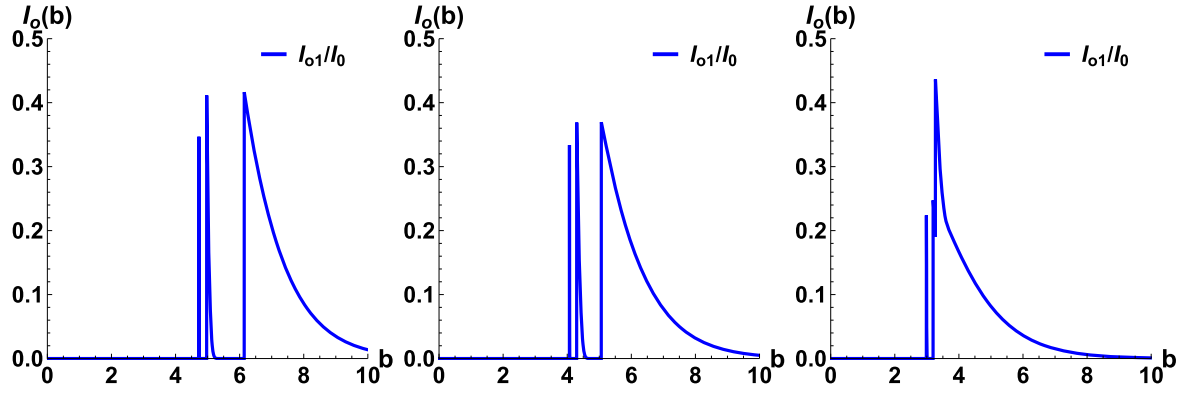

(d) $Io, \alpha = 0.3$ (e) $Io, \alpha = 0.6$ (f) $Io, \alpha = 0.8$

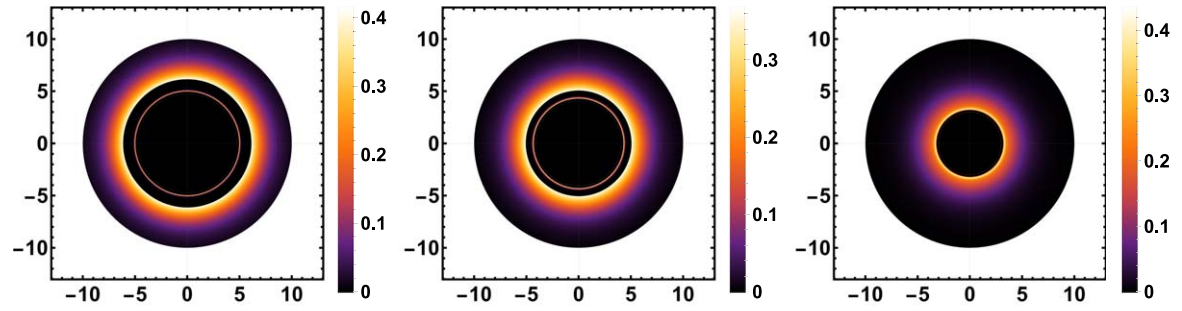

(g) $\alpha = 0.3$,ring (h) $\alpha = 0.5$,ring (i) $\alpha = 0.8$,ring

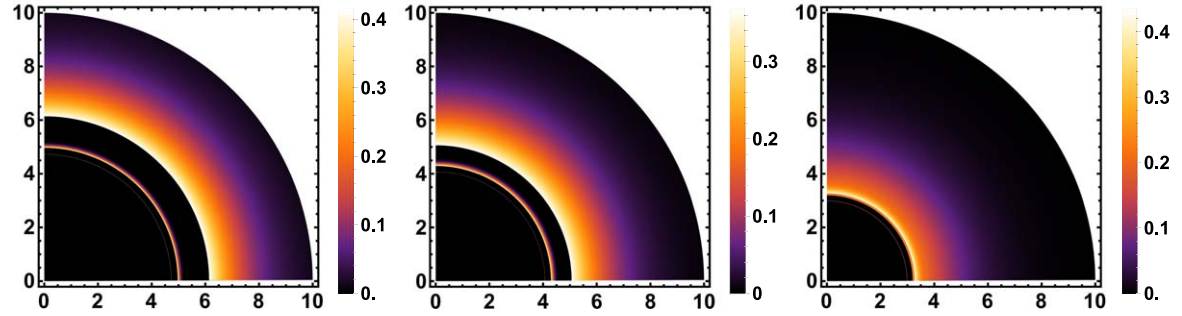

(j) $\alpha = 0.3$,ring structure (k) $\alpha = 0.6$,ring structure (l) $\alpha = 0.8$,ring structure

Figure 5. Observational appearance of a thin disk in an exponential model with $\alpha = 0.3$, 0.6 and 0.8 and fixed $M = 1$.

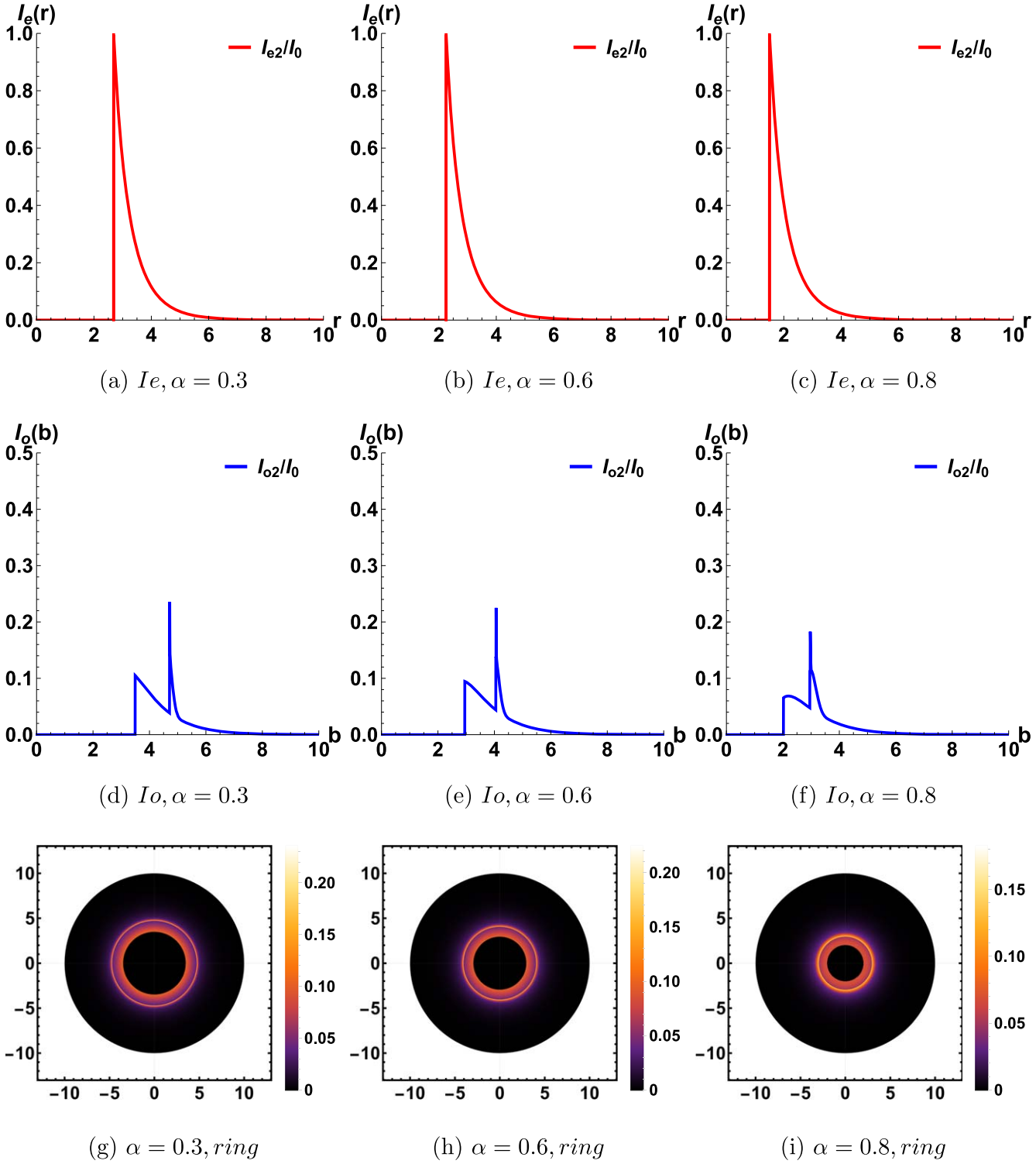

(a) $Ie, \alpha = 0.3$ (b) $Ie, \alpha = 0.6$ (c) $Ie, \alpha = 0.8$

(d) $Io, \alpha = 0.3$ (e) $Io, \alpha = 0.6$ (f) $Io, \alpha = 0.8$

(g) $\alpha = 0.3, ring$ (h) $\alpha = 0.6, ring$ (i) $\alpha = 0.8, ring$

Figure 6. Observational appearances of a thin disk in the power-law exponential model with $\alpha = 0.3$, 0.6 and 0.8 and fixed $M = 1$.

4.2.4. GLM model. The radiative intensity profile of the accretion disk is characterized using Johnson's standard unbounded model as a parameterization method, which has been previously employed in the literature within the context of reproducing general relativistic magnetohydrodynamic simulations of the accretion flow. We focus on the Gralla–Lupsasca–Marrone (GLM) model, and the radiation intensity profile of the GLM model reads as [63]

$$I_{\rm GLM} = \frac{e^{-\frac{1}{2}[\gamma + \operatorname{arcsinh}(\frac{r-\alpha}{\sigma})]}}{\sqrt{(r-\alpha)^2 + \sigma^2}}. \tag{29}$$

This model assumes monochromatic emission (in the frame of the disk) characterized by three variable parameters: α, which is associated with the position of the emission peak and tends

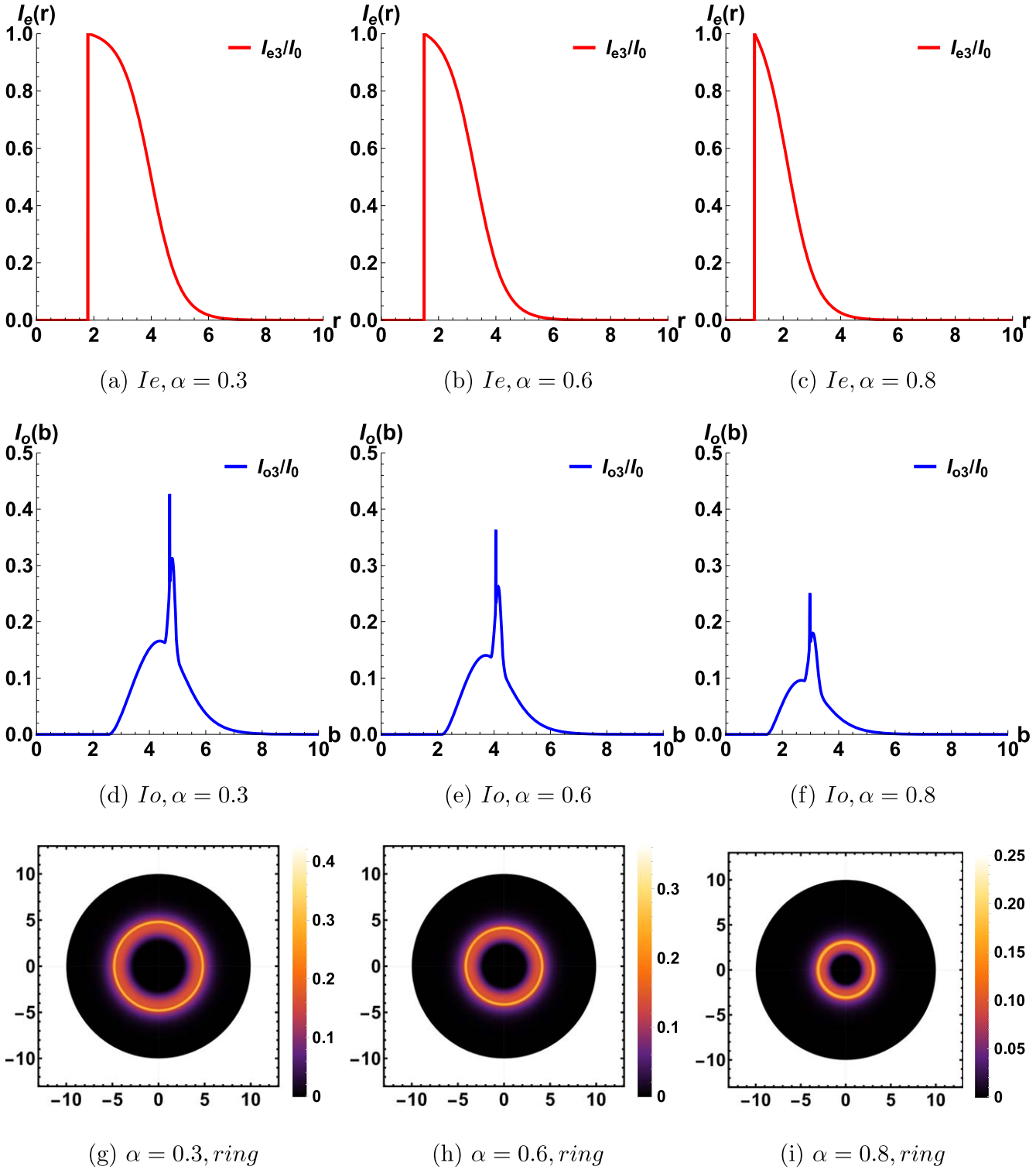

(a) $Ie, \alpha = 0.3$ (b) $Ie, \alpha = 0.6$ (c) $Ie, \alpha = 0.8$

(d) $Io, \alpha = 0.3$ (e) $Io, \alpha = 0.6$ (f) $Io, \alpha = 0.8$

(g) $\alpha = 0.3, ring$ (h) $\alpha = 0.6, ring$ (i) $\alpha = 0.8, ring$

Figure 7. Observational appearances of a thin disk in the bell-shaped model with $\alpha = 0.3$, 0.6 and 0.8 and fixed $M = 1$.

to shift the peak away from (or behind) the horizon for small (or large) values; γ, which controls the asymmetry of the profile, with negative (or positive) values favoring the positioning of the steeper part of the profile at the horizontal line (or outer side); σ (usually in units of M), which is related to the width of the outline, with small (or large) values often resulting in steeper (or wider) decay and narrower (or broader) rings.

Thus, for this work, one can choose the GLM model [55] with $\gamma = -2$, $\alpha = 17/3$ and $\sigma = 1/4$. Specific intensities I_{e_4}/I_0 are shown in figures 8(a)–(c). They are the same because I_e does not concern α, and the specific observational

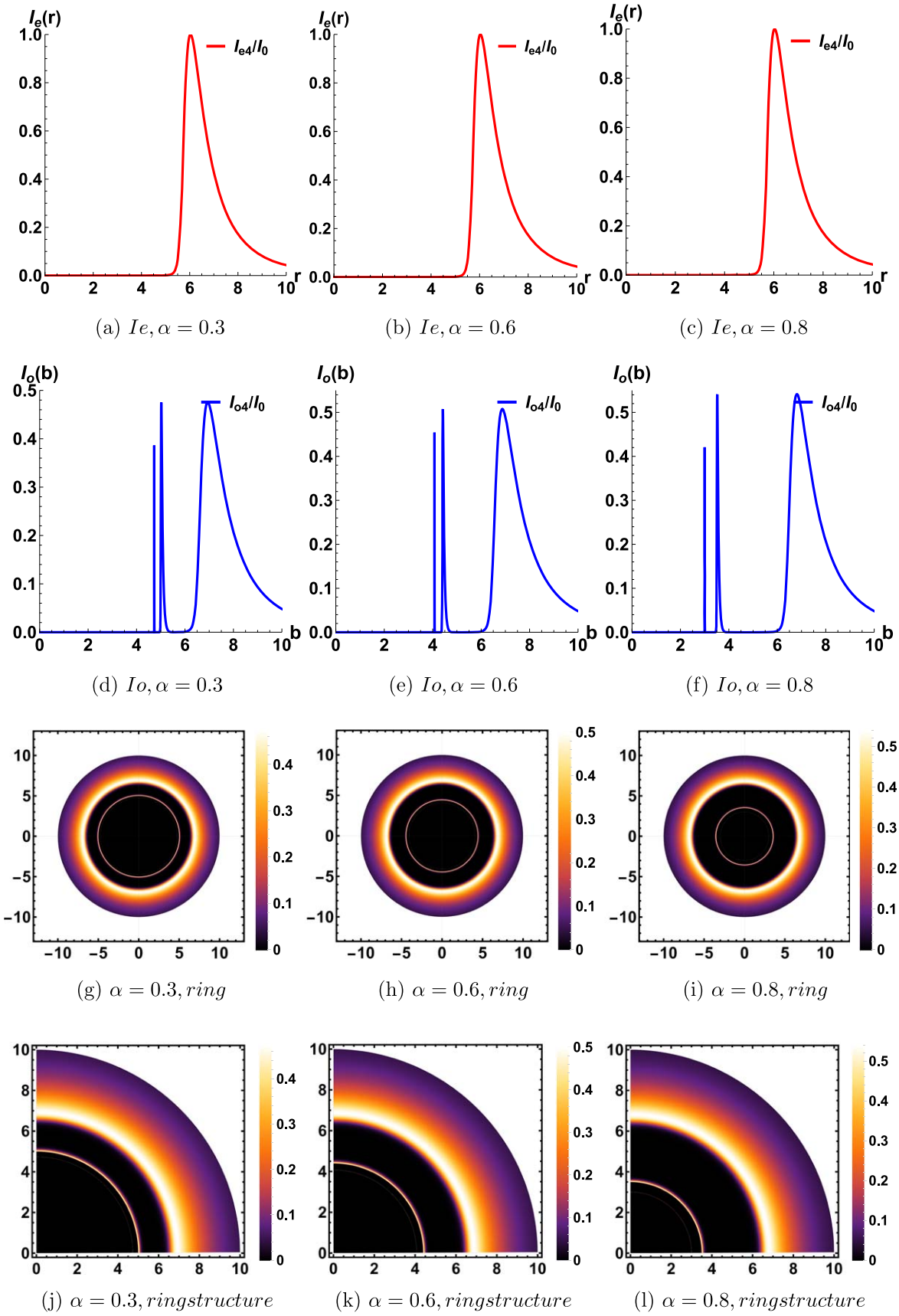

(a) $Ie, \alpha = 0.3$ (b) $Ie, \alpha = 0.6$ (c) $Ie, \alpha = 0.8$

(d) $Io, \alpha = 0.3$ (e) $Io, \alpha = 0.6$ (f) $Io, \alpha = 0.8$

(g) $\alpha = 0.3, ring$ (h) $\alpha = 0.6, ring$ (i) $\alpha = 0.8, ring$

(j) $\alpha = 0.3, ringstructure$ (k) $\alpha = 0.6, ringstructure$ (l) $\alpha = 0.8, ringstructure$

Figure 8. Observational appearances of a thin disk in the GLM3 model with $\alpha = 0.3$, 0.6 and 0.8 and fixed $M = 1$, $\mu = 17/4$, $\gamma = -2$ and $\sigma = 0.25$.

intensities are demonstrated in figures 8(d)–(f). Note that in this model there are three peaks in each observational intensity corresponding to direct emission, the lensing ring and the photon ring respectively, which indicates that the three intensities are independent of each other and do not have superposition effects. The diagrams with respect to the special intensities are shown in figures 8(g)–(i), and the accretion structures are shown in figures 8(j)–(l). Similar to figure 5, the difference between the GLM model and the exponential model is that the direct emission rises and decays more moderately, causing the outermost ring to be brighter than in the exponential model; this is stable and does not change with α. One can also notice an extremely narrow ring of $n = 3$ inside the sub-ring (lensing ring) by magnification but, interestingly, this photon ring moves further away from the lensing ring with increasing α.

5. Conclusion and discussion

In this paper, we first derive the metric of the hairy black hole in WEC, and the hairy parameter α is interpreted as the matter sector independent of the global charge [45]. Angular momentum (L) and energy (E) are derived, and the impact parameter is defined as $b \equiv L/E$. Through numerical integration, we obtain the trajectories of photons and compare the images for different values of α. We observe that when the hairy parameter α increases, the ability of the black hole to deflect photons continuously decreases. Subsequently, we examine $r_{\rm ISCO}$ for hairy black holes and calculate its variation with α, which represents the minimum radius of stable orbits for massive particles.

Subsequently, the backward ray-tracing method is employed to investigate the hairy black hole shadow observed under spherical accretion. We study the emission intensity from the stationary spherical accretion. For simplicity, we assume that the emitted light frequency obeys a normal distribution and the photon density follows a logarithmic normal distribution. Then an examination of the redshift factor (g) and the infinitesimal proper line element is undertaken, ultimately deriving the integral formula for the observer's received light intensity. We simulated the projection of the shadow of stationary spherical accretion and the projection of spherical accretion under infalling conditions on the observer's screen. As a result, we observed that the overall light intensity for both types of spherical accretion decreases with an increase in the hairy parameter α. Under the same α, the light intensity for infalling is significantly lower than that for stationarity, attributed to the Doppler effect in the emission of infalling accretion material.

For a distant observer, the thin disk model is considered to be a theoretical model consistent with observed facts. In this sense, incident photons from the accretion disk can orbit the black hole a varying number of times before leaving the black hole, so that they may generate several light rings that confine the shadow. We investigate the classification of photon orbits, namely, direct emission, lensing ring and photon ring, and distinguish these three types of photon trajectories in the geodesic images. We summarize the relationship between emitted light intensity and the intensity observed. As the number of intersections between photons and the accretion disk increases, the light intensity received by the observer increases. Therefore, we sum the intensities and introduce the transfer function $r_n(b)$, depicting their profiles. The slopes of these images are referred to as demagnification factors. These ring images are presented in all four toy models. Next, considering the four models, we found that all four models consistently report a reduction in the size of the rings with increasing hairy parameter α. It is also observed that when the emission peaks occur at $r_{\rm ph}$ and $r_{\rm h}$, a coupling of three rings dominated by direct emission and the lensing ring becomes significant. Specifically, as the peak is at $r_{\rm ph}$ (power-law exponential model), the contribution of the lensing ring is minimal, while when the peak is at $r_{\rm h}$ (bell-shaped model), the contribution of the lensing ring is significantly enhanced. The most prominent result we found is that when the emission peaks occur at $r_{\rm ISCO}$ and beyond (e.g. as mentioned at $r = 17/3$), one can clearly observe decoupled rings for $n = 1$, 2 and 3, especially the very fine $n = 3$ (photon ring) on the innermost side, which coincides with the expectations of the EHT discoveries.

With the improvement in astrophysical observation precision, rings with $n = 2$ and $n = 3$ may be detected by future detectors. This holds significant importance for validating the strong gravitational field predicted by general relativity.

Acknowledgments

The authors are grateful to We Hong, Shangyu Wen, Aoyun He and Xuetao Yang for useful discussions and insightful suggestions. This work is supported by the National Natural Science Foundation of China (NSFC) with grant nos 12175212, 12275183 and 12275184. This work was finished on the server from Kun-Lun in Center for Theoretical Physics, School of Physics, Sichuan University.

References

[1] Akiyama K *et al* 2022 First Sagittarius A* Event Horizon Telescope results. I. the shadow of the supermassive black hole in the center of the Milky Way *Astrophys. J. Lett.* **930** L12
[2] Akiyama K *et al* 2022 First Sagittarius A* Event Horizon Telescope results. II. EHT and multiwavelength observations, data processing, and calibration *Astrophys. J. Lett.* **930** L13
[3] Akiyama K *et al* 2022 First Sagittarius A* Event Horizon Telescope results. III. imaging of the galactic center supermassive black hole *Astrophys. J. Lett.* **930** L14
[4] Akiyama K *et al* 2022 First Sagittarius A* Event Horizon Telescope results. IV. variability, morphology, and black hole mass *Astrophys. J. Lett.* **930** L15
[5] Akiyama K *et al* 2022 First Sagittarius A* Event Horizon Telescope results. V. testing astrophysical models of the galactic center black hole *Astrophys. J. Lett.* **930** L16

[6] Akiyama K *et al* 2022 First Sagittarius A* Event Horizon Telescope results. VI. testing the black hole metric *Astrophys. J. Lett.* **930** L17

[7] Akiyama K *et al* 2019 First M87 Event Horizon Telescope results. I. the shadow of the supermassive black hole *Astrophys. J. Lett.* **875** L1

[8] Akiyama K *et al* 2019 First M87 Event Horizon Telescope results. II. array and instrumentation *Astrophys. J. Lett.* **875** L2

[9] Akiyama K *et al* 2019 First M87 Event Horizon Telescope results. III. data processing and calibration *Astrophys. J. Lett.* **875** L3

[10] Akiyama K *et al* 2019 First M87 Event Horizon Telescope results. IV. imaging the central supermassive black hole *Astrophys. J. Lett.* **875** L4

[11] Akiyama K *et al* 2019 First M87 Event Horizon Telescope results. V. physical origin of the asymmetric ring *Astrophys. J. Lett.* **875** L5

[12] Akiyama K *et al* 2019 First M87 Event Horizon Telescope results. VI. the shadow and mass of the central black hole *Astrophys. J. Lett.* **875** L6

[13] Shoom A A 2017 Metamorphoses of a photon sphere *Phys. Rev.* D **96** 084056

[14] Synge J L 1966 The escape of photons from gravitationally intense stars *Mon. Not. R. Astron. Soc.* **131** 463–6

[15] Bardeen J M, Press W H and Teukolsky S A 1972 Rotating black holes: Locally nonrotating frames, energy extraction, and scalar synchrotron radiation *Astrophys. J.* **178** 347

[16] Luminet J P 1979 Image of a spherical black hole with thin accretion disk *Astron. Astrophys.* **75** 228–35 https://ui.adsabs.harvard.edu/abs/1979A%26A....75..228L/abstract

[17] Dokuchaev V I and Natalia N O 2019 The brightest point in accretion disk and black hole spin: implication to the image of black hole M87 *Universe* **5** 183

[18] Dokuchaev V I and Nazarova N O 2020 Visible shapes of black holes M87* and SgrA* *Universe* **6** 154

[19] Wen S, Hong W and Tao J 2023 Observational appearances of magnetically charged black holes in Born–Infeld electrodynamics *Eur. Phys. J.* C **83** 277

[20] He A, Tao J, Wang P, Xue Y and Zhang L 2022 Effects of Born–Infeld electrodynamics on black hole shadows *Eur. Phys. J.* C **82** 683

[21] Mou P-H, Chen Y-X, He K-J and Li G-P 2022 Shadows and observational appearance of a new family of Ayón–Beato–García black holes *Commun. Theor. Phys.* **74** 125401

[22] Guo G, Wang P, Wu H and Yang H 2022 Quasinormal modes of black holes with multiple photon spheres *J. High. Enery Phys.* JHEP06(2022)060

[23] Chen Y, Guo G, Wang P, Wu H and Yang H 2022 Appearance of an infalling star in black holes with multiple photon spheres *Sci. China Phys. Mech. Astron.* **65** 120412

[24] Guo G, Lu Y, Wang P, Wu H and Yang H 2023 Black holes with multiple photon spheres *Phys. Rev.* D **107** 124037

[25] Guo G, Jiang X, Wang P and Wu H 2022 Gravitational lensing by black holes with multiple photon spheres *Phys. Rev.* D **105** 124064

[26] Zeng X-X, He K-J, Li G-P, Liang E-W and Guo S 2022 QED and accretion flow models effect on optical appearance of Euler–Heisenberg black holes *Eur. Phys. J.* C **82** 764

[27] Zeng X-X and Zhang H-Q 2020 Influence of quintessence dark energy on the shadow of black hole *Eur. Phys. J.* C **80** 1058

[28] Zeng X-X, He K-J and Li G-P 2022 Effects of dark matter on shadows and rings of brane-world black holes illuminated by various accretions *Sci. China Phys. Mech. Astron.* **65** 290411

[29] Yang X 2024 Observational appearance of the spherically symmetric black hole in PFDM *Phys. Dark Univ.* **44** 101467

[30] Han S-Z, Jiang J, Zhang M and Liu W-B 2020 Photon sphere and phase transition of d-dimensional ($d \geqslant 5$) charged Gauss–Bonnet AdS black holes *Commun. Theor. Phys.* **72** 105402

[31] Karshiboev K, Atamurotov F, Abdujabbarov A, Övgün A and Reyimberganov A 2024 Exploring the shadow of a rotating charged ModMax black hole *Commun. Theor. Phys.* **76** 025401

[32] Li G-P and He K-J 2021 Observational appearances of a $f(R)$ global monopole black hole illuminated by various accretions *Eur. Phys. J.* C **81** 1018

[33] Meng Y, Kuang X-M, Wang X-J, Wang B and Wu J-P 2023 Images from disk and spherical accretions of hairy Schwarzschild black holes *Phys. Rev.* D **108** 064013

[34] Volonteri M 2010 Formation of supermassive black holes *Astron. Astrophys. Rev.* **18** 279–315

[35] Herdeiro C A R and Eugen R 2015 Asymptotically flat black holes with scalar hair: a review *Int. J. Mod. Phys.* D **24** 1542014

[36] Penrose R 1965 Gravitational collapse and space-time singularities *Phys. Rev. Lett.* **14** 57–9

[37] Penrose R 1969 Gravitational collapse: the role of general relativity *Riv. Nuovo Cim.* **1** 252–76

[38] Blandford R D and Znajek R L 1977 Electromagnetic extractions of energy from Kerr black holes *Mon. Not. R. Astron. Soc.* **179** 433–56

[39] Ovalle J 2008 Searching exact solutions for compact stars in braneworld: a conjecture *Mod. Phys. Lett.* A **23** 3247–63

[40] Randall L and Sundrum R 1999 A large mass hierarchy from a small extra dimension *Phys. Rev. Lett.* **83** 3370–3

[41] Morales E and Tello-Ortiz F 2018 Compact anisotropic models in general relativity by gravitational decoupling *Eur. Phys. J.* C **78** 841

[42] Panotopoulos G and Rincón Á 2018 Minimal geometric deformation in a cloud of strings *Eur. Phys. J.* C **78** 851

[43] Las Heras C and León P 2019 New algorithms to obtain analytical solutions of Einstein's equations in isotropic coordinates *Eur. Phys. J.* C **79** 990

[44] Maurya S K and Tello-Ortiz F 2020 Charged anisotropic compact star in $f(R, T)$ gravity: a minimal geometric deformation gravitational decoupling approach *Phys. Dark Univ.* **27** 100442

[45] Avalos R, Bargueño P and Contreras E 2023 A static and spherically symmetric hairy black hole in the framework of the gravitational decoupling *Fortsch. Phys.* **71** 2200171

[46] Ovalle J, Posada C and Stuchlík Z 2019 Anisotropic ultracompact Schwarzschild star by gravitational decoupling *Class. Quant. Grav.* **36** 205010

[47] Ovalle J, Casadio R, Contreras E and Sotomayor A 2021 Hairy black holes by gravitational decoupling *Phys. Dark Univ.* **31** 100744

[48] Ovalle J 2019 Decoupling gravitational sources in general relativity: the extended case *Phys. Lett.* B **788** 213–8

[49] Ovalle J 2017 Decoupling gravitational sources in general relativity: from perfect to anisotropic fluids *Phys. Rev.* D **95** 104019

[50] Cedeño F X L and Contreras E 2020 Gravitational decoupling in cosmology *Phys. Dark Univ.* **28** 100543

[51] Maurya S K, Tello-Ortiz F and Ray S 2021 Decoupling gravitational sources in $f(R,T)$ gravity under class I spacetime *Phys. Dark Univ.* **31** 100753

[52] Cavalcanti R T, Alves K D S and da Silva J M H 2022 Near-horizon thermodynamics of hairy black holes from gravitational decoupling *Universe* **8** 363

[53] Zhang C-M, Zhang M and Zou D-C 2023 Gravitational decoupling for hairy black holes in asymptotic AdS spacetimes *Chin. Phys.* C **47** 015106

[54] Gao X-J, Sui T-T, Zeng X-X, An Y-S and Hu Y-P 2023 Investigating shadow images and rings of the charged Horndeski black hole illuminated by various thin accretions *Eur. Phys. J.* C **83** 1052

[55] Dias da Silva L F, Lobo F S N, Olmo G J and Rubiera-Garcia D 2023 Photon rings as tests for alternative spherically symmetric geometries with thin accretion disks *Phys. Rev.* D **108** 084055
[56] Jiang H-X, Mizuno Y, Fromm C M and Nathanail A 2023 Two-temperature GRMHD simulations of black hole accretion flows with multiple magnetic loops *Mon. Not. R. Astron. Soc.* **522** 2307–24
[57] Johnson M D *et al* 2020 Universal interferometric signatures of a black hole's photon ring *Sci. Adv.* **6** eaaz1310
[58] Tiede P, Johnson M D, Pesce D W, Palumbo D C M, Chang D O and Galison P 2022 Measuring photon rings with the ngEHT *Galaxies* **10** 111
[59] Jefremov P I, Tsupko O Y and Bisnovatyi-Kogan G S 2015 Innermost stable circular orbits of spinning test particles in Schwarzschild and Kerr space-times *Phys. Rev.* D **91** 124030
[60] Gralla S E, Holz D E and Wald R M 2019 Black hole shadows, photon rings, and lensing rings *Phys. Rev.* D **100** 024018
[61] Zeng X-X, Zhang H-Q and Zhang H 2020 Shadows and photon spheres with spherical accretions in the four-dimensional Gauss–Bonnet black hole *Eur. Phys. J.* C **80** 872
[62] Wang X-J, Kuang X-M, Meng Y, Wang B and Wu J-P 2023 Rings and images of Horndeski hairy black hole illuminated by various thin accretions *Phys. Rev.* D **107** 124052
[63] Gralla S E, Lupsasca A and Marrone D P 2020 The shape of the black hole photon ring: a precise test of strong-field general relativity *Phys. Rev.* D **102** 124004